

Fault gouge evolution and its dependence on normal stress and rock strength—Results of discrete element simulations: Gouge zone properties

Yonggui Guo¹ and Julia K. Morgan¹

Received 22 May 2006; revised 9 December 2006; accepted 18 June 2007; published 5 October 2007.

[1] In order to study the process of gouge zone evolution, and its dependence on normal stress, σ_n , and uniaxial compressive strength, σ_{ucs} , we simulate the breakdown of fault blocks and growth of fault gouge zones using the distinct element method (DEM) in two dimensions. Breakable elastic bonds were added between adjacent, closely packed particles to generate the fault blocks with a given σ_{ucs} ranging from 100 to 260 MPa. DEM experiments were conducted by shearing the fault blocks along an initially flat surface for a range of σ_n from 10 to 100 MPa. The simulated fault gouge zones experience two distinct stages of evolution, i.e., fast growth and slow growth, distinguished by a switch in deformation mechanism from dominantly wear of the fault blocks to dominantly shearing of existing fault gouge. The rate of the gouge zone thickening decreases exponentially during the fast growth stage (to about 20% shear strain, i.e., 7.4 mm shear displacement) and then reaches a relatively constant value, marking the beginning of the slow growth stage. The thickening rate increases with increasing σ_n and decreasing σ_{ucs} during the fast growth stage, but the dependency reverses during the slow growth stage. The mean grain size of the gouge shows a first-order dependence on shear displacement, and varies less significantly with σ_n and σ_{ucs} . In our simulated shear zones that undergo both surface wear and grain comminution, gouge grains develop power law size distributions characterized by a two-dimensional fractal dimension D ranging from 0.6 to 2.4.

Citation: Guo, Y., and J. K. Morgan (2007), Fault gouge evolution and its dependence on normal stress and rock strength—Results of discrete element simulations: Gouge zone properties, *J. Geophys. Res.*, 112, B10403, doi:10.1029/2006JB004524.

1. Introduction

[2] Natural faults at shallow depths undergo continual wear of fault surfaces during slip, which leads to a progressive increase in the thickness of the fault gouge zone with net slip [Scholz, 1987; Power *et al.*, 1988]. In the meantime, gouge microstructure and grain characteristics (i.e., grain shape, size, and size distribution) vary with fault shear displacement as a result of grain reorganization and comminution [Marone and Scholz, 1989; Beeler *et al.*, 1996]. These changes in gouge zone features during fault deformation may affect fault strength, stability, and earthquake characteristics [e.g., Byerlee and Summers, 1976; Sammis *et al.*, 1986; Marone *et al.*, 1990; Beeler *et al.*, 1996; Heermance *et al.*, 2003]. The effects of fault gouge on fault zone behavior have been studied extensively, both experimentally and numerically under a wide range of conditions [e.g., Engelder *et al.*, 1975; Marone and Scholz, 1989; Morrow and Byerlee, 1989; Beeler *et al.*, 1996; Mora and Place, 1998, 1999; Morgan and Boettcher, 1999; Morgan, 1999; Mair *et al.*, 2002; Guo and Morgan, 2004; Anthony and Marone, 2005; Guo and

Morgan, 2006]. The dependence of strength and stability of the fault on fault gouge properties, however, remains poorly constrained, because gouge properties change progressively during frictional sliding, and are also dependent on many factors, such as wall rock strength, confining pressure (i.e., depth), and shear displacement [Engelder, 1974; Anderson *et al.*, 1980, 1983; Sammis and Osborne, 1982; Scholz, 1987].

[3] Studies of natural fault zones have yielded many important observations on the nature of fault gouge. It was found that fault gouge develops characteristic shear fabrics [Rutter *et al.*, 1986; Chester and Logan, 1987], and gouge grains obey either a nonfractal [Wilson *et al.*, 2005] or a fractal size distribution characterized by a fractal dimension D in a range of 1.7 to 5.52 [Sammis *et al.*, 1987; Blenkinsop, 1991; An and Sammis, 1994; Storti *et al.*, 2003; Billi *et al.*, 2003; Rawling and Goodwin, 2003]. These observations are important to infer the mechanical processes of gouge formation [Sammis *et al.*, 1987; Wilson *et al.*, 2005], the frictional and mechanical effects of gouge [Storti *et al.*, 2003; Monzawa and Otsuki, 2003], fault zone stress state, and deformation history [Lin, 2001; Rawling and Goodwin, 2003]. However, such field studies can only capture the properties of fault gouge at a single evolutionary stage and therefore offer limited information about the dynamic processes of gouge zone evolution.

¹Department of Earth Science, Rice University, Houston, Texas, USA.

[4] Important insights for understanding the effects of variations in gouge properties on fault behavior during fault growth are provided by fault process studies in the laboratory. By shearing experimental faults with artificial gouge, laboratory experiments demonstrate that fault gouge affects the stability of slip [e.g., *Byerlee and Summers*, 1976; *Scholz et al.*, 1972], and the transition from stable to unstable sliding appears to be related to many factors, including gouge grain shape [*Mair et al.*, 2002], grain size [*Dieterich*, 1981], grain size distribution [*Biegel et al.*, 1989], gouge thickness [*Byerlee and Summers*, 1976; *Anthony and Marone*, 2005], composition [*Morrow et al.*, 1992; *Saffer et al.*, 2001; *Saffer and Marone*, 2003], and the shear localization features [*Byerlee et al.*, 1978; *Logan et al.*, 1979; *Tullis et al.*, 1989; *Beeler et al.*, 1996]. Because of limitations in laboratory conditions, short shear displacements prevent the natural formation of thick gouge layers. Artificial fault gouge is usually introduced between shearing wall rocks in the laboratory experiments. Consequently, the frictional and mechanical effects of sliding surface wear and continual growth of gouge zone on fault slip are excluded or limited in these types of experimental studies.

[5] Numerical simulations of fault zone deformation can also provide insights about the role of fault gouge in evolving faults. By shearing circular or irregularly shaped grains (i.e., fault gouge) in a configuration similar to direct shear laboratory experiments, numerical experiments have shown that the strength of simulated fault zones is correlated with gouge grain configuration [*Mora and Place*, 1998, 1999], grain size distribution [*Morgan*, 1999], and grain shape [*Morgan*, 1999; *Guo and Morgan*, 2004]. In addition, recent simulations of granular shear using the distinct element method (DEM) also demonstrate that gouge grain comminution can either strengthen or weaken the granular shear zone, depending on the competing effects of reduced frictional resistance by fracturing and changes in grain characteristics by comminution [*Guo and Morgan*, 2006]. Again, in these numerical simulations, fault gouge is created artificially rather than by the progressive break down of wall rocks.

[6] Recognizing the importance of evolving structural and physical properties of fault gouge for understanding its frictional and mechanical effects on fault zone sliding, and therefore earthquake processes, we carry out DEM experiments in two dimensions to simulate the break down of fault blocks and the evolution of fault gouge zones, starting from bare rock surfaces. The purpose of this study is (1) to map out the spatial and temporal distribution of deformation, gouge grain characteristics, and structures that develop within the gouge as it deforms; (2) to examine the variation of gouge properties (i.e., gouge zone thickness, porosity, gouge grain size, and size distribution) with shear displacement; and (3) to investigate the dependency of gouge zone evolution on normal stress σ_n and rock uniaxial compressive strength σ_{ucs} . This paper is focused on the physical characteristics and structural properties of our simulated fault gouges. Their frictional and micromechanical properties are described in the companion paper (Y. Guo and J. K. Morgan, Fault gouge evolution and its dependence on normal stress and rock strength: Results of discrete element simulations: Gouge zone micromechanics, submitted to *Journal of Geophysical Research*, 2006, hereinafter

referred to as Guo and Morgan, submitted manuscript, 2006). The data presented in these two papers may help to understand the processes of gouge zone development and their stabilizing effects on fault zones.

2. Numerical Methods

[7] Our numerical experiments were carried out using the DEM technique [*Cundall and Strack*, 1979]. DEM was designed originally to determine the mechanical behavior of assemblies of discrete particles. Particle interactions occur only at contacts and particle motion is determined using Newton's second law of motion. In this study, we generate fault blocks from assemblages of circular particles of different sizes, connected by elastic bonds [*Guo and Morgan*, 2004, 2006]. Each bond acts as two elastic springs and an elastic beam that transmit contact normal force F_n , shear force F_s , and moment M , respectively (Figure 1). The forces and moment acting on the bond are proportional to bond normal stiffness k_n or shear stiffness k_s , and also proportional to bond cross-sectional area A or the moment of inertia of the bond cross section I , respectively, i.e.,

$$F_n = k_n A \delta_n \quad (1)$$

$$F_s = k_s A \delta_s \quad (2)$$

$$M = k_n I \theta \quad (3)$$

$$A = \pi R^2 \quad (4)$$

$$I = \frac{1}{4} A R^2 \quad (5)$$

where δ_n , δ_s , and θ are the relative normal, shear, and angular displacements of the particles at the contact, respectively. R is the effective radius determined from the radius of the two contacting particles, R_1 and R_2 , given by

$$R = \frac{2R_1 R_2}{R_1 + R_2} \quad (6)$$

A bond breaks if the bond tensile stress, σ , equals or exceeds the bond tensile strength σ_{\max} , or if the shear stress, τ , equals or exceeds the bond shear strength τ_{\max} , i.e.,

$$\sigma = \frac{F_n}{A} + \frac{|M|}{I} R > \sigma_{\max} \quad (7)$$

$$\tau = \frac{|F_s|}{A} > \tau_{\max} \quad (8)$$

Here, we assume that the tensile normal force is positive. When one of the above failure criteria is satisfied, bonded particle pairs lose their cohesion and become unbonded.

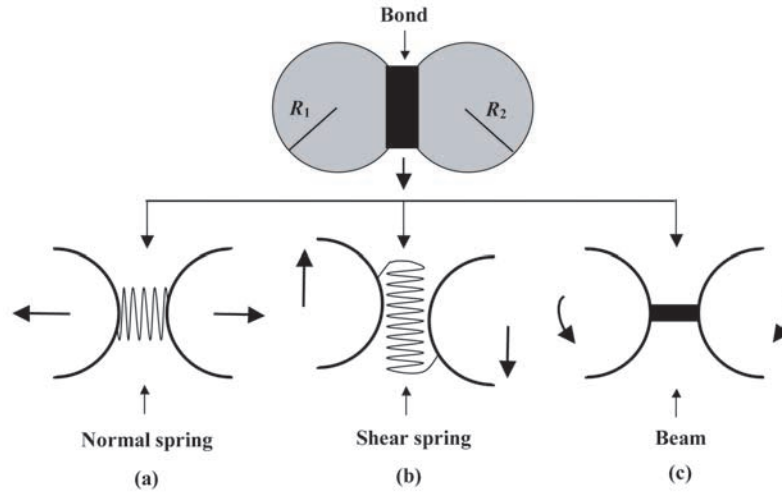


Figure 1. Schematic diagram of interparticle bond and its mechanical analogs (modified after *Guo and Morgan* [2004]). The bond between particles behaves as (a and b) two elastic springs that generate and transmit normal and shear forces, respectively, and (c) an elastic beam that transmits moment. The interparticle bonds are assumed to deform in a linear elastic manner within the failure criteria while the bonded particles are displaced and rotated from their equilibrium positions.

[8] For unbonded particles in contact, the contact force is calculated using a nonlinear Hertz-Mindlin contact model

$$F_n = \left(\frac{2G\sqrt{2R}}{3(1-\nu)} \right) \delta_n^{3/2} \quad (9)$$

$$F_s = \left(\frac{2[3RG^2(1-\nu)]^{1/3}}{(2-\nu)} \right) F_n^{1/3} \delta_s \quad (10)$$

where G is the shear modulus and ν is Poisson's ratio [Mindlin and Deresiewicz, 1953; Johnson, 1985; Morgan and Boettcher, 1999; Guo and Morgan, 2004]. The contact undergoes frictional sliding when F_s exceeds the critical shear force F_s^{\max} for slip, as calculated by

$$F_s^{\max} = \mu_p F_n \quad (11)$$

where μ_p is interparticle friction defined in Table 1. Other numerical details are identical to those described by Morgan and Boettcher [1999] and Guo and Morgan [2004].

3. Experimental Design

[9] Fault blocks are constructed by randomly generating 8588 circular particles of four different sizes within a two-dimensional (2-D) domain (Figure 2 and Table 1). In order to create a closely packed particle assemblage, the domain is compressed under an isotropic confining pressure of 100 MPa until an equilibrium stress state is reached. The confining pressure is then decreased gradually to 6 Pa where the distance between particle surfaces S between adjacent particles is minimal. S is defined by

$$S = \left(\sum_n |l - R_i - R_j| \right) / n \quad (12)$$

where n is the number of adjacent particle pairs, and l is center distance between two adjacent particles with radius equal to R_i and R_j , respectively. Elastic bonds with uniform properties are added between adjacent particles (Table 1) if $|l - R_i - R_j|$ is smaller than a given threshold (0.001% of the radius of the smallest particle). A few particles ($\sim 4\%$) do not satisfy this criterion, so they do not have bonds and behave as noncemented particles in pore spaces. The resulting block of bonded particles, with a height of 36 mm, equates to cemented rock (Figure 2). A flat fault surface is defined in the middle of the block by deleting bonds between particles if lines connecting their centers cross the central line of the block. Top and bottom layers of particles (shown in gray) represent fault zone boundaries (Figure 2). They transmit stress during fault zone deformation, but move at constant velocities without damage.

[10] Initial particle size in our generated fault blocks follows a fractal distribution described by a power law defined with a fractal dimension D . The D value is given by the following relationship [Turcotte, 1986; Sammis et al.,

Table 1. Parameters for Numerical Experiments

Parameter	Value
Experimental variables	
Shear strain rate, s^{-1}	2.88×10^{-8}
Total shear strain	200% (i.e., 74 mm shear displacement)
Applied normal stress, MPa	10, 25, 40, 55, 70, 100
Particle properties	
Initial assemblage porosity, %	15
Size in radius, mm	0.3, 0.25, 0.2083, 0.1736
Mean size in area, mm^2	0.1636
Size distribution D	1.0
Interparticle friction	0.5
Shear modulus, GPa	29
Poisson's ratio	0.20
Interparticle bond properties	
Poisson's ratio	0.20
Young's modulus, GPa	69.6

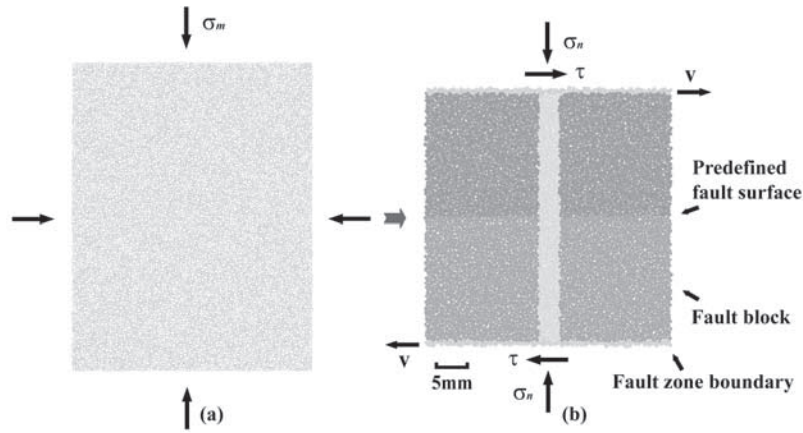


Figure 2. Experimental design. (a) Particle assemblage compressed under a high confining pressure σ_m . The pressure σ_m is then decreased gradually to a near zero value. (b) Rock generated by adding elastic bonds between adjacent particles (see text for details). Top and bottom layers of grey particles are defined as fault zone boundaries. A flat fault surface is predefined in the middle of the rock by deleting bonds across the surface as indicated by color contrast. Deformation is induced under constant normal stress σ_n and variable shear stress τ by moving the top boundary to the right and the bottom boundary to the left at constant velocity v . The shaded vertical column is strain marker.

1986, 1987; Morgan and Boettcher, 1999; Guo and Morgan, 2004]:

$$D = \log(N_{i+1}/N_i) / \log(R_i/R_{i+1}) \quad (13)$$

where N_{i+1} and N_i are numbers of particles with a radius equal to $R_i + 1$ and R_i , respectively. D value is set to 1 in our fractal size fault block. Particle sizes are given in Table 1.

[11] Cohesive strength for most rocks is typically 1–2 times the tensile strength [e.g., Attewell and Farmer, 1976]. In our bond strength definition, we chose τ_{\max} to be 1.27 times greater than σ_{\max} (Table 2), consistent with our previous study [Guo and Morgan, 2006]. Fault blocks were deformed in a uniaxial compressive configuration to determine their strengths. Five sets of bond strengths were employed to yield σ_{ucs} values of fault blocks in a range from 100 to 260 MPa (Table 2), comparable to strengths ranging from that of sandstone to granite [Attewell and Farmer, 1976]. In order to study the separate effects of σ_{ucs} and σ_n on gouge zone evolution, one suite of experiments involved shearing five pairs of fault blocks with different values of σ_{ucs} under a σ_n of 25 MPa, and a second suite involved shearing the fault blocks with σ_{ucs} of 183 MPa under σ_n of 10, 40, 55, 70, and 100 MPa. All of the pairs of fault blocks were generated from the exact same initial particle assemblage. The experiments carried out to examine the effects of σ_{ucs} are labeled using the letter C (i.e., compressive strength), followed by the σ_{ucs} value for the fault blocks, and the experiments conducted to explore the effects of σ_n are labeled using the letter N (i.e., normal stress), followed by the applied experimental value for σ_n . Therefore N25 and C183 refer to the same experiment that is carried out at normal stress of 25 MPa by shearing the fault block with σ_{ucs} value of 183 MPa.

[12] DEM experiments were conducted by moving the upper fault zone boundary to the right and the bottom to the left, at constant and equal velocities, while maintaining σ_n on the boundaries. A periodic boundary condition is applied

in the horizontal direction, i.e., when a particle leaves the domain from the right boundary, it reenters through the left boundary, or vice versa. In this deformation configuration, the maximum principal stress σ_1 and the least principal stress σ_3 fluctuate around orientations approximately 45° and 135° to the fault surface, respectively. The total shear strain for each experiment is 200% (i.e., 74 mm shear displacement). The deformation state of the fault zone was recorded at each 2% shear strain increment (i.e., 0.74 mm shear displacement increment), yielding stress state, gouge deformation mechanisms (i.e., translation, rotation, sliding, and fracture), gouge zone thickness, gouge porosity, gouge grain size, and size distribution statistics.

4. Deformation Visualization and Gouge Zone Analysis

[13] In order to visualize shear zone deformation, we plot grain size, particle rotation, and particle shear displacement gradient for each 2% shear strain. Representative plots are shown in Figures 3–5. Particle rotations and displacements in our numerical experiments can be synthetic (i.e., in the

Table 2. Mechanical Properties of Fault Blocks in Numerical Experiments

Experiment ^a	Bond Strength, MPa		Uniaxial Compressive Strength, MPa
	Tensile	Shear	
C100	143	182	100
C140	206.25	262.5	140
C183 (N25), N10, N40, N55, N70, N100	275	350	183
C220	332.75	423.5	220
C260	393.25	500.5	260

^aC refers to fault block compressive strength, and N refers to experimental normal stress. The number behind the C or N is either the fault block compressive strength or applied normal stress of represented experiment.

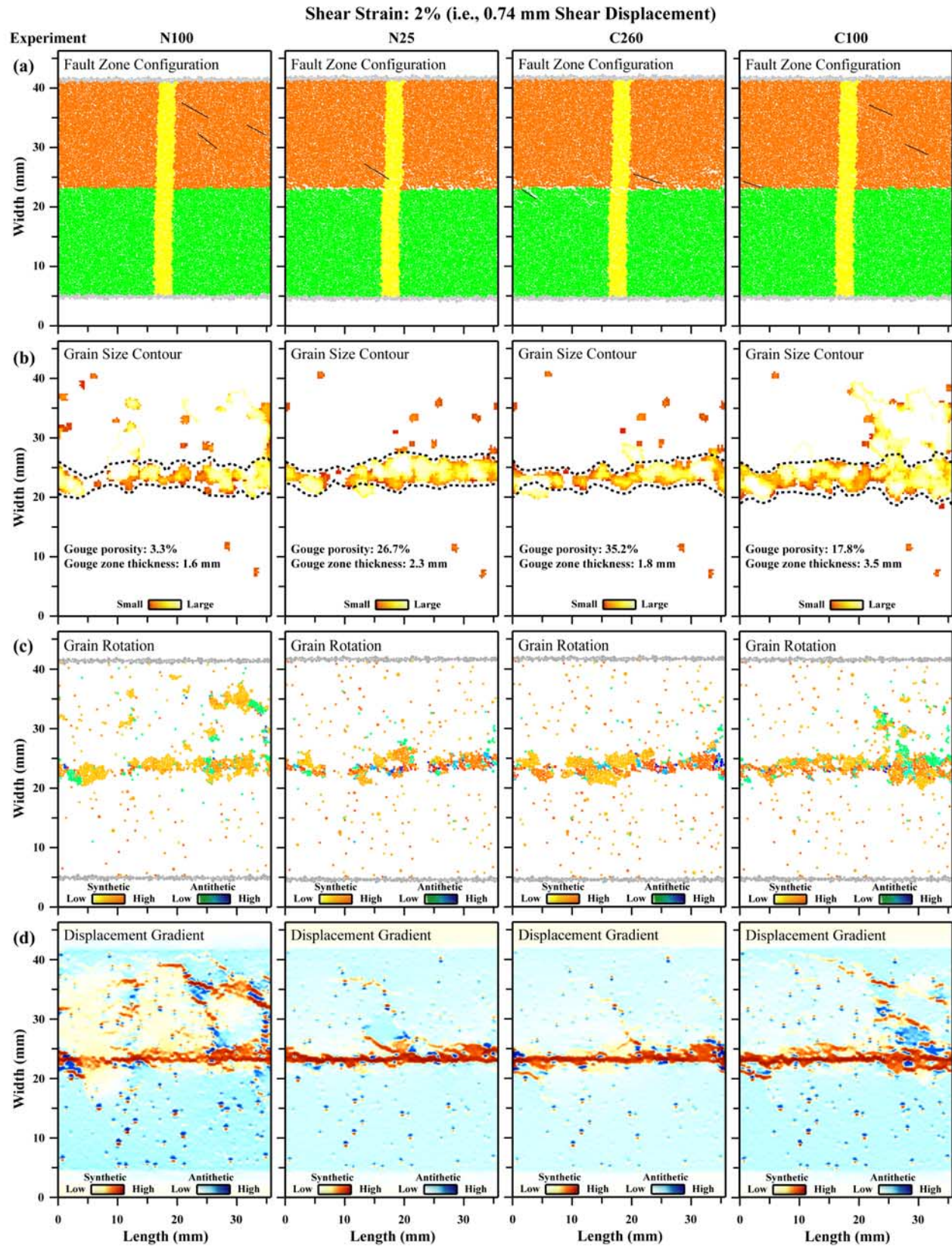


Figure 3

same sense as the fault block displacement) or antithetic (i.e., in an opposite direction). To better resolve the regions undergoing intense shear deformation, we calculate the gradient of particle shear displacement as the directional derivative of the horizontal particle displacement [e.g., *Morgan and Boettcher*, 1999]. Grains are defined as single particles or clusters of bonded particles that are not connected to the fault blocks or the fault zone boundaries by bonds, due either to their initial configuration or to bond breakage during deformation. In our simulated shear zones, the grains are found either within damaged zones in the fault blocks or between the fault surfaces (Figures 3b–5b). In the first case, the grains undergo minimal rotation or slip after formation and are not part of the gouge zone. Here, we define gouge grains as those that experience repeated high-magnitude rotation or translation within a high-displacement gradient zone. The gouge zone boundaries are interpreted based on this definition of fault gouge (Figures 3b–5b).

[14] Changes in volume, ΔV , (i.e., area in two dimensions) of our simulated shear zones during deformation results primarily from variations in the volume of the gouge zone as a result of dilation, compaction, gouge grain comminution, and rearrangement, and secondarily from variations in the volume of the damaged fault blocks as a result of opening and closing of fractures and elastic compression and decompression of the fault blocks (Figures 3a–5a). As the latter contribution is small, we assume that volume change only occurs in the gouge zone; therefore gouge porosity η_g and gouge zone thickness T can be calculated approximately by the following equations, respectively:

$$\eta_g = \{1 - A_g / [\Delta V + (A_g/A_p)V_o]\} 100\% \quad (14)$$

$$T = [A_g / (1 - \eta_g/100)] / L \quad (15)$$

where A_g is the area of the gouge grains and A_p is the area of all particles that constitute the fault blocks. These are the actual areas occupied only by circular particles and do not include the void space between them. V_o is the original area of the fault blocks including void space, and L is the length of the fault blocks, which remains constant.

[15] Grain size analysis of the gouge includes (1) the calculation of mean grain size, given by the ratio of A_g to the number of gouge grains, and (2) the calculation of grain radius, i.e., the radius of an equivalent circular area for a given grain shape. Because of numerical limitations on initial particle size, our simulated gouge zones are composed of a limited number of gouge grains and grain sizes. To best represent this narrow size distribution, we compare

the cumulative grain abundance against grain radius to quantify the fractal dimension D , i.e.,

$$D = \log[(N_{i+1}/N_i) + 1] / \log(R_i/R_{i+1}) \quad (16)$$

where R_i is greater than R_{i+1} .

5. Results

[16] Our simulated shear zones show two distinct stages of gouge zone development: a fast growth stage (i.e., rapid gouge zone thickening) and slow growth stage (i.e., slower gouge zone thickening), which sets in once a well developed gouge zone has formed. The transition from the fast growth stage to the slow growth stage occurs at about 20% shear strain (i.e., 7.4 mm shear displacement) for most experiments, varying slightly with σ_n and σ_{ucs} . Each evolutionary stage exhibits characteristic fabrics, micromechanical behavior, and distinct σ_n and σ_{ucs} dependence of gouge zone evolution. In order to show the principal features of simulated gouge zone evolution, we present snapshots of the deforming gouge zones for four representative experiments (i.e., C100, C260, N25, and N100) at 2%, 20%, and 200% shear strain (i.e., 0.74, 7.4, and 74 mm shear displacement) (Figures 3–5). The effects of σ_n and σ_{ucs} on gouge zone development are then demonstrated by comparing the intrinsic properties of the gouge zone for each suite of experiments, i.e., gouge porosity, gouge zone thickness, mean grain size, and grain size distribution.

5.1. Characteristics of Gouge Zone Evolution

[17] In general, all of the numerical experiments show similar characteristics of gouge zone evolution with slight variations in their details. The qualitative behavior of our simulated faults can be described as a function of the dimensionless ratio of σ_n to σ_{ucs} . The four experiments shown in Figures 3–5, N100, C100, N25, and C260, have σ_n/σ_{ucs} ratios of 0.55, 0.25, 0.14, and 0.1, respectively.

[18] During the fast growth stage, the fault surfaces become separated by a thin gouge zone. During this stage, shear strain is accommodated primarily by wear of the fault surfaces (i.e., plucking of grains from the sliding surfaces) and gouge grain comminution, and secondarily, by the development of fractures within the fault blocks. Other deformation mechanisms, such as grain rolling and sliding, become more significant as the fault gouge accumulates. The typical deformation fabrics developed during this stage are failure surfaces in the fault blocks inclined to the fault zone boundary. These general observations can be seen in the snapshots of shear zone deformation at 2% shear strain for all experiments (e.g., Figure 3).

[19] At 2% shear strain, the higher σ_n/σ_{ucs} ratio experiments, N100 and C100, are characterized by higher compaction, lower gouge zone porosity, and longer fractures in

Figure 3. Snapshot of gouge zone evolution at 2% shear strain (i.e., 0.74 mm shear displacement) for experiments N100, N25, C260, and C100. (a) Fault zone configuration. The red or green color of a particle denotes its origin in either the upper or lower fault block. Yellow particles define vertical strain markers. Black lines denote the orientation and length of distinct fractures, i.e., wide void spaces in linear arrangements. (b) Gouge grain size contour. Dotted lines are the interpreted gouge zone boundaries (see text for details). (c) Incremental particle rotation over 2% shear strain. White indicates no rotation. (d) Directional derivative of the horizontal component of the residual displacement [*Morgan and Boettcher*, 1999].

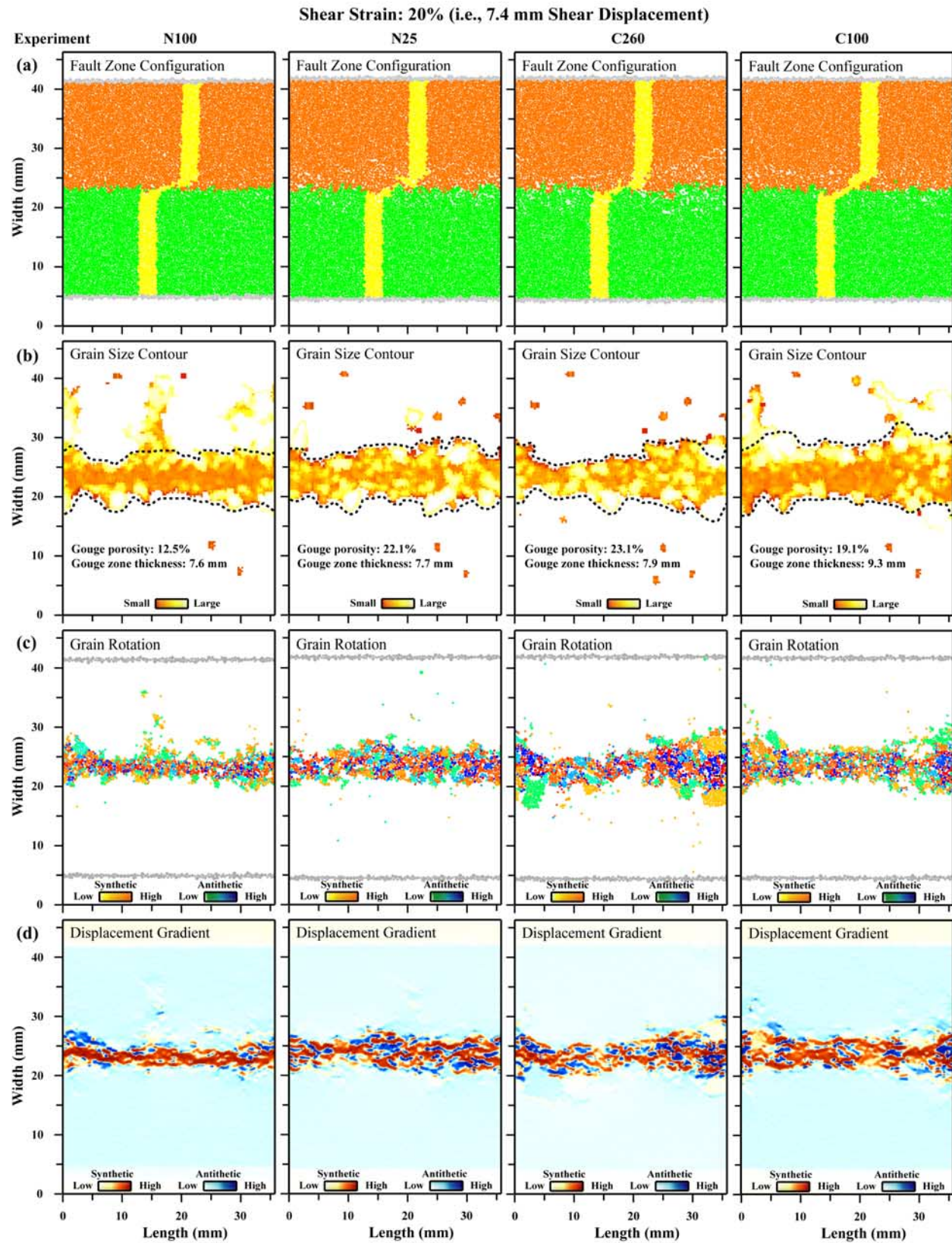


Figure 4. Snapshot of gouge zone evolution at 20% shear strain (i.e., 7.4 mm shear displacement) for experiments N100, N25, C260, and C100. Same as in Figure 3.

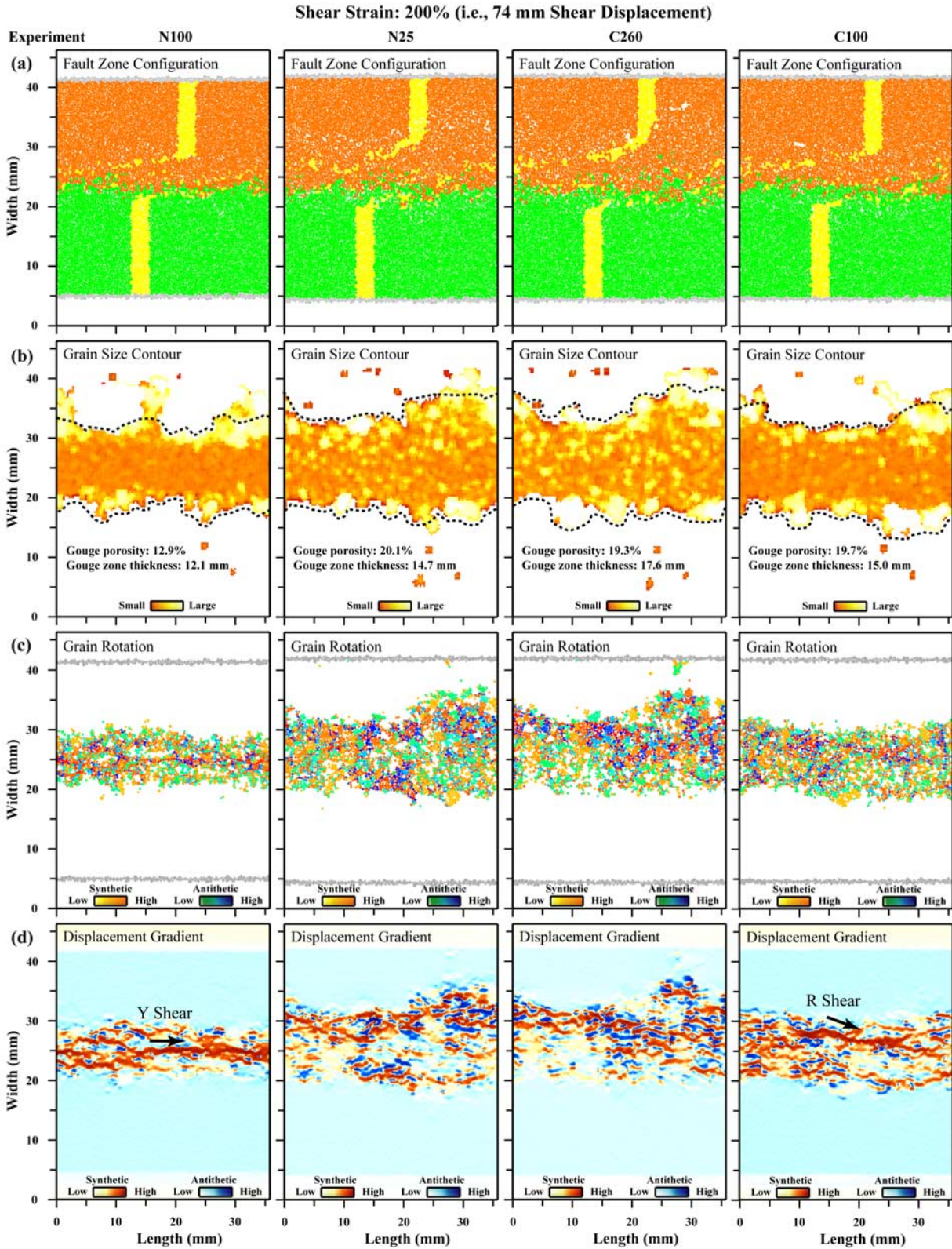


Figure 5. Snapshot of gouge zone evolution at 200% shear strain (i.e., 74 mm shear displacement) for experiments N100, N25, C260, and C100. Same as in Figure 3. Y shear and R shear are indicated by horizontal and low-angle synthetic slip zones, respectively, shown in red color in Figure 5d. Arrows show the orientations of shears. They are parallel to Y and R shears, respectively. The presence of lateral periodic boundaries results in the yellow displacement markers not being greatly offset relative to each other, even though the shear strain is 200%.

the fault blocks, particularly the upper block (Figure 3a). These fractures are recognized by linear arrangements of voids (Figure 3a), modest grain rotation (Figure 3c), and localized slip (i.e., red bands in Figure 3d). Their orientations are around 45° to fault zone boundary, generally parallel or subparallel to σ_1 . Displacement along the fault surfaces is minimal (i.e., little distortion of the yellow strain marker). For the lower σ_n/σ_{ucs} ratio experiments, N25 and C260, in contrast, the fault zone exhibits higher dilation, higher porosity within the gouge zone, higher magnitudes of gouge grain rotation, and larger shear displacement along fault surfaces (Figures 3a, 3c, and 3d). The interiors of the fault blocks experience very little damage, except close to the fault surfaces where inclined fractures develop (Figure 3d). The fractures typically initiate at interlocked asperities and propagate into the fault blocks (Figure 3a). Correlated high-displacement gradients in the fractured areas indicate that some shear strain is accommodated by slip along these fractures (Figure 3d).

[20] The transition from the fast growth to the slow growth stage at about 20% shear strain coincides with a decrease in deformation within the fault blocks, as shown by rare fractures and fracture-related grain rotations and sliding (Figure 4). More strain is accommodated within the gouge zone by grain comminution, rolling and sliding. In the higher σ_n/σ_{ucs} ratio experiments, N100 and C100, the gouge zone undergoes compaction and gouge grains exhibit little vertical mixing, i.e., the boundary between red and green particles remains relatively flat (Figure 4a). The middle of the gouge zone is characterized by concentrations of smaller grains that exhibit the most significant rotation and sliding (Figures 4b–4d). Larger grains along the edges of the gouge zone arise from grains newly plucked from the boundaries of the gouge zone. The zone of high shear strain is very narrow, and localized within the fine-grained gouge (Figure 4d). In contrast, the gouge zones in the lower σ_n/σ_{ucs} ratio experiments, N25 and C260, are more porous. The boundary between red and green particles becomes irregular, as grains translate vertically and mix (Figure 4a). Grain size distribution in the gouge zone is more heterogeneous, as smaller grains are scattered among the big grains (Figure 4b). Deformation, i.e., by grain rolling and contact sliding, is more distributed (Figures 4c and 4d).

[21] The slow growth stage, which initiates at $\sim 20\%$ for all experiments, continues to the 200% shear strain limit. The initially flat fault surfaces generally become rough, and are separated by a well developed gouge zone (Figure 5). The rate of fracturing within the fault blocks, the wear rate of the fault surfaces, and the intensity of gouge grain comminution all decrease significantly with increasing shear displacement. Shear strain is mainly accommodated within the gouge zone by grain rolling and sliding. Gouge zone properties are more heterogeneous, for example, grain size is greater and porosity is higher along the gouge zone boundaries. Common shear fabrics seen in natural or experimental fault gouge, such as discrete boundary shears, low-angle synthetic R shears, and horizontal Y shears [e.g., Logan *et al.*, 1979, 1992; Marone and Scholz, 1989; Marone *et al.*, 1990; Gu and Wong, 1994; Beeler *et al.*, 1996; Morgan and Boettcher, 1999], are well developed in the gouge zone (Figure 5d).

[22] For the higher σ_n/σ_{ucs} ratio experiments, N100 and C100, highly comminuted small gouge grains of relatively uniform size (i.e., relative well sorted) are distributed within the gouge zone, while large grains recently plucked from the fault surfaces are scattered along the gouge zone boundaries (Figure 5b). Deformation is minor within the fault blocks, and intense and heterogeneous within the gouge zone. Grains distributed along well developed slip zones within the gouge show the highest magnitude of rotation, mostly in a synthetic sense (Figure 5c). A distinct long horizontal slip zone (i.e., Y shear) and a distinct low-angle slip zone (i.e., synthetic R shear) are developed in N100 and C100, respectively. Slip zones are less well developed along the gouge zone boundaries (Figure 5d).

[23] For the lower σ_n/σ_{ucs} ratio experiments, N25 and C260, grain size in the interior of the gouge zone falls within a wider range (i.e., relatively poorly sorted), and, on average, is greater. Large grains occur along the gouge zone boundaries (Figure 5b), but are few in number. Many grains show high-magnitude synthetic or antithetic rotations (Figure 5c). Shear strain is distributed across the gouge zone, and the wide range of grain sizes tends to favor the development of short oblique and subhorizontal slip zones; synthetic slip zones (red) are well developed close to the more irregular upper gouge zone boundary (Figure 5d).

[24] In addition, for the high σ_n experiment, N100, the gouge zone at 200% shear strain is highly compacted, as indicated by reduced fault zone thickness compared to those in other experiments (Figure 5a). Gouge porosity is about 12%, lower than that of the original fault blocks (15%). For the low σ_n experiments, N25, C100, and C260, gouge porosities are similar, around 20%, higher than that of the original fault blocks.

5.2. Gouge Zone Porosity and Thickness

[25] The ratios of σ_n to σ_{ucs} are in a range from 0.1 to 0.25 for the experiments carried out under σ_n of 25 MPa, while the ratios for those conducted under different σ_n range from 0.055 to 0.55. Consequently, normal stress variations result in a wider range of porosity (Figure 6) and thickness values (Figure 7). Within the first 4% shear strain, gouge porosities calculated using equation (14) increase or decrease in response to the initial dilation or compaction and the opening or closing of failure surfaces (Figure 6). With continued shear strain, the effects of fault block fracture on porosity become much less significant; the gouge porosities for all experiments decrease nonlinearly, and eventually settle out to fluctuate around near constant values. Except for high σ_n experiments N100 and N75, the gouge porosities in our simulated shear zones are higher than that of the initial fault blocks (15%). Gouge porosity depends on both σ_n and σ_{ucs} ; generally, porosity decreases with increasing σ_n (Figure 6a), and with decreasing σ_{ucs} (Figure 6b). One characteristic where normal stress and bond strength have different effects is in the compaction of well-developed gouge zones that have many unbreakable single particle grains. Bond strength has no effect on these grains. In contrast, normal stress controls their packing and therefore porosity and thickness.

[26] As noted in Figures 3–5, the thickness of the simulated gouge zone varies significantly with shear displacement (Figure 7). All of the experiments show a rapid increase in gouge zone thickness within the first 20% or less

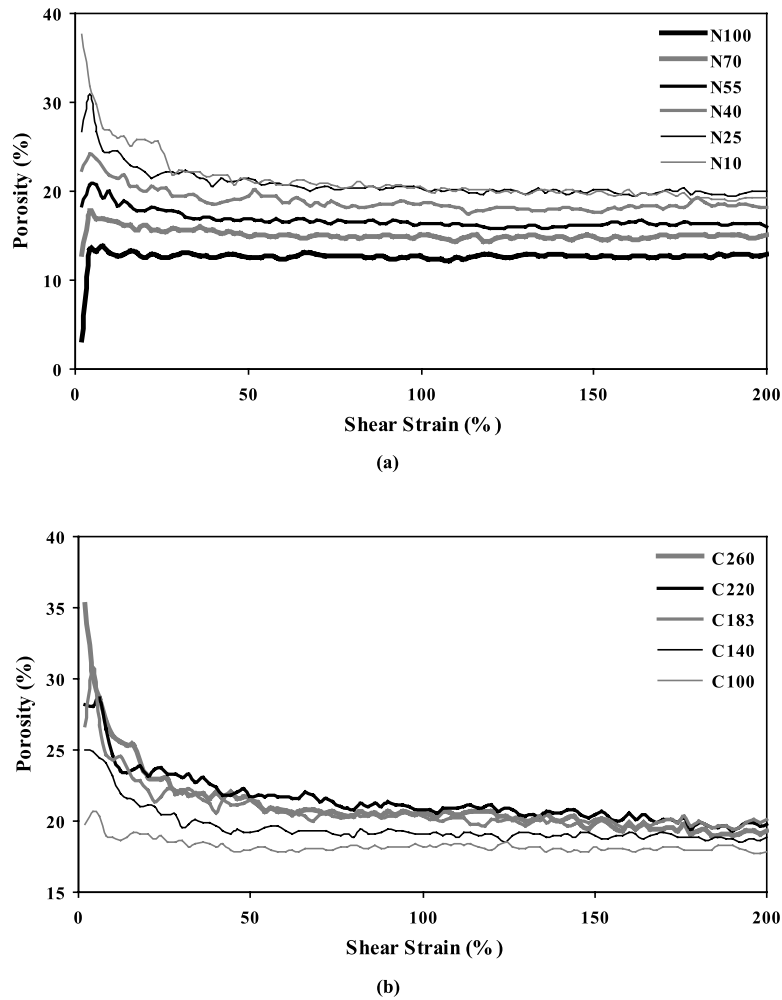


Figure 6. Effects of (a) normal stress and (b) uniaxial compressive strength on gouge porosity plotted against shear strain.

shear strain, i.e., the fast growth stage. Gouge zone thickness then increases at a much lower rate with continued shear displacement. The evolution of gouge zone thickness is also strongly dependent on both σ_n and σ_{ucs} . Within the first 20% shear strain, experiment N100 shows the most rapid increase in gouge zone thickness. The rate of gouge thickening decreases with decreasing σ_n , with the exception of experiment N40, which shows an anomalously low rate of thickening. During the slow growth stage, the rate of gouge thickening tends to decrease with increasing σ_n (Figure 7a). Experiment N10 shows the greatest rate of increase in the gouge zone thickness during this stage. The dependence of gouge zone thickness on σ_{ucs} is similar to the change in σ_n , but in the opposite direction (Figure 7b). For example, experiment C100 shows the fastest gouge growth rate within the first 20% shear strain, while experiment C260 shows the highest rate of increase over the last 180% shear strain. The rate of the gouge zone thickening appears to decrease with increasing σ_{ucs} within the first 20% shear strain, but increase with increasing σ_{ucs} over the remaining shear strain.

5.3. Gouge Grain Size and Size Distribution

[27] Mean gouge grain size also evolves systematically with shear strain for all experiments (Figure 8). In general,

mean grain size reaches its peak value within the first 4% shear strain of each experiment, and then falls exponentially with increasing shear strain. Both σ_n and σ_{ucs} have secondary effects on the mean gouge grain size (Figure 8). Averaged mean gouge grain size over 200% shear strain tends to decrease with increasing σ_n and with decreasing σ_{ucs} , but varies within a very narrow range in response to variations in these parameters (Figure 8 insets). The one anomaly in this pattern is experiment C260 in which mean grain size is noticeably higher than in the other experiments at 200% shear strain, and about 2 times larger than the mean particle size of the initial particle assemblage (Figure 8b).

[28] Grain size variations with shear strain correlate with shear zone thickness trends, indicating changes in processes responsible for grain size evolution associated with growth stages. Thus the evolution of grain size distribution with shear displacement is a sensitive indicator of mechanical processes of gouge deformation. A representative plot of cumulative grain abundance versus equivalent grain radius for experiment N25 shows generally linear increases in $\log(\text{cumulative grain abundance})$ with decreasing $\log(\text{grain size})$ (Figure 9). This observation suggests that grain size follows a fractal size distribution as demonstrated by others [Sammis *et al.*, 1987; Marone and Scholz, 1989; Biegel *et al.*,

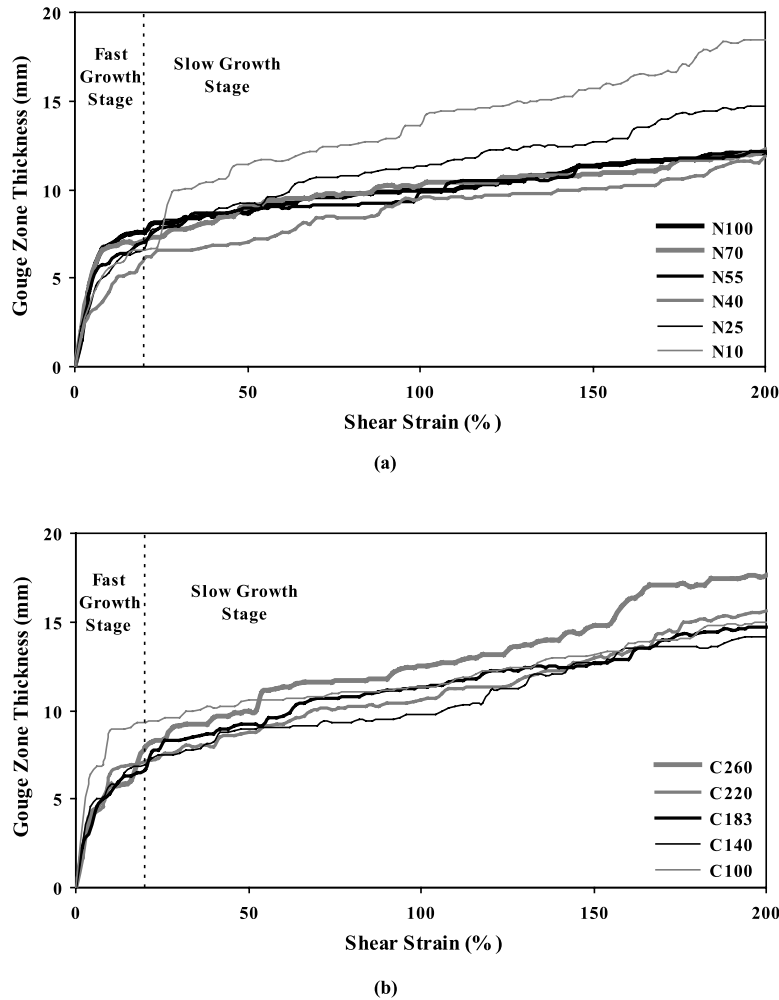


Figure 7. Effects of (a) normal stress and (b) uniaxial compressive strength on gouge zone thickness plotted against shear strain.

1989; Blenkinsop, 1991; An and Sammis, 1994; Storti *et al.*, 2003; Billi *et al.*, 2003; Rawling and Goodwin, 2003; Abe and Mair, 2005], and can be quantified by the fractal dimension D (equation (16)).

[29] In this particular case, crushing of gouge grains is the only mechanism for grain size reduction, resulting in progressive steepening of particle size distribution (PSD) curve. At the same time, the total abundance of gouge grains increases, shifting the curve upward. The grain size distribution curves can be divided into a linear portion to the right and a nonlinear portion to the left. The linear portion describes the distribution of large grain sizes (i.e., radius >2.8 mm) where grains are still breakable, and a reliable indicator of grain size distribution. The nonlinear portion includes both breakable and unbreakable grains. The nonlinearity results from the accumulation of unbreakable grains (i.e., single particles), and is not a good measure of grain size evolution, as would natural gouges undergo continued comminution. To eliminate the effect of unbreakable grains on the size distribution, D values defined by equation (16) were calculated from the best fit to the linear portion of the gouge grain size distribution.

[30] As demonstrated by the representative experiment N25 (Figure 10), D values of our simulated fault gouges

generally increase during the fast growth stage (Figure 10) as grains are added to the gouge zone. D values then vary in a wide range from 0.9 to 2.4, but occasionally reaching plateaus that last as long as 20% shear strain. Both σ_n and σ_{ucs} affect surface wear and grain comminution processes and therefore the D values. No systematic variation in the mean D value of the slow growth stage is observed with either σ_n or σ_{ucs} in our numerical experiments (Figure 10 insets).

6. Discussion

6.1. Structural Evolution of Fault Zones

[31] Our numerical experiments demonstrate that shear zones show different stages of structural evolution, yielding different gouge zone characteristics and controlling mechanisms. Specifically, we observe a fast growth stage up to $\sim 20\%$ shear strain (i.e., 7.4 mm shear displacement), and a slow growth stage throughout the remaining 180% shear strain (i.e., 66.6 mm shear displacement). These two stages are distinguished by a change in the dominant deformation structures from tensile fractures within the fault blocks early during fault slip, to slip zones accommodating slip within well-developed fault gouge zones later during the simulations.

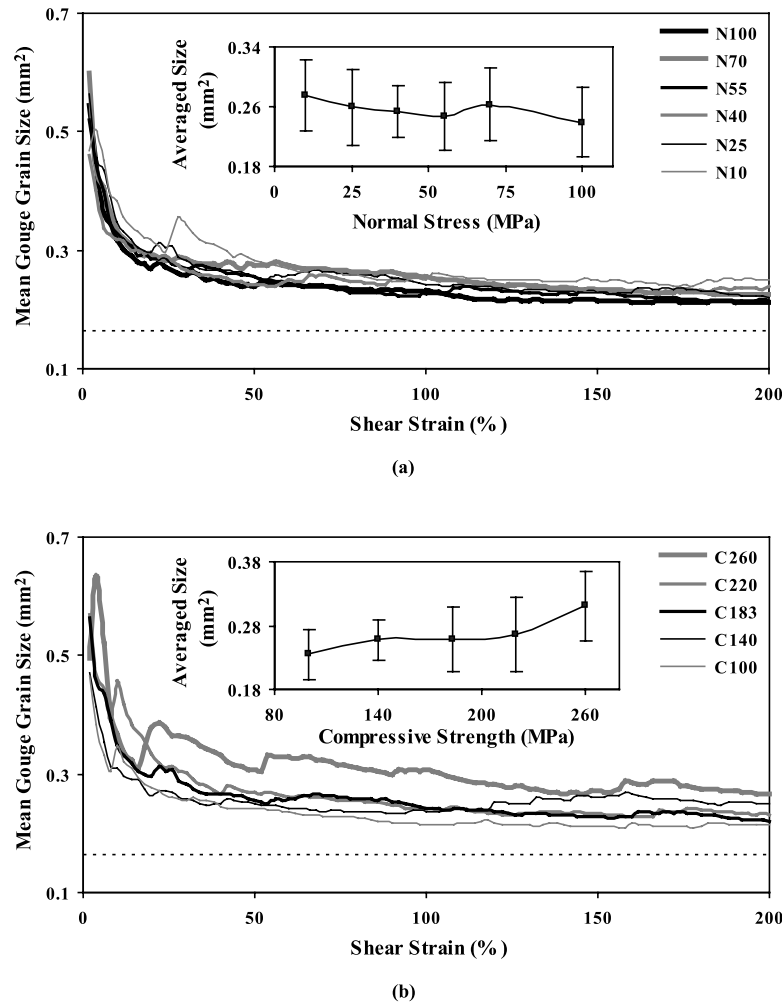


Figure 8. Effects of (a) normal stress and (b) uniaxial compressive strength on mean grain size plotted against shear strain. Dotted lines denote the mean particle size of the initial particle assemblage (Figure 2a). Insets show averaged mean grain size over 200% shear strain. Error bars show the standard deviation. Interpolated lines are fit to data points by eye.

[32] In our numerical experiments, the earliest phase of the fast growth stage is characterized by the development of inclined fractures in the fault blocks, subparallel to the predicted σ_1 (Figure 3a). Since high σ_n and low σ_{ucs} favor such brittle deformation, the longest and most abundant fractures are observed in those experiments. Similar tensile fractures are also common features in simple shear configurations during initial shearing of natural faults and lab samples [Knipe and White, 1979; Scholz, 1990; Wibberley *et al.*, 2000].

[33] Once the gouge zones in our numerical experiments reach a sufficient thickness to completely separate the opposing fault surfaces, the slow growth stage initiates, generally after $\sim 20\%$ shear strain (i.e., 7.4 mm shear displacement). At this point, the dominant deformation mechanism changes from damage (i.e., fracturing and wear) of fault blocks, to shearing within the well-developed fault gouge zone. The shearing of gouge grains produces heterogeneously distributed slip zones, such as R shears and Y shears, in the gouge zones (Figure 5d). In well-developed, naturally occurring or simulated gouge zones, such defor-

mation is also characterized by the development of characteristic shear fabrics within the fault gouge [e.g., Logan *et al.*, 1979, 1992; Marone and Scholz, 1989; Marone *et al.*, 1990; Gu and Wong, 1994; Beeler *et al.*, 1996; Morgan and Boettcher, 1999]. However, only rarely are the initial stages of this gouge development preserved.

[34] Our experiments also reveal that the types and geometries of the slip zones that develop during shearing are strongly dependent on gouge grain sorting, i.e., the distribution of gouge grain sizes about the mean. Visual inspection of grain size distribution in the interiors of the gouge zones at 200% shear strain (i.e., 74 mm shear displacement) shows that sorting increases with increasing σ_n and with decreasing σ_{ucs} (Figure 5b). This is because large grains are readily crushed under these high-stress and low-strength conditions. Concurrently, fault block damage and plucking is suppressed. With increasing grain sorting induced by the different stress and strength conditions, the slip zones within the gouge zones change from short curved zones defining distributed deformation fields, to short oblique linear zones, then to long oblique linear surfaces,

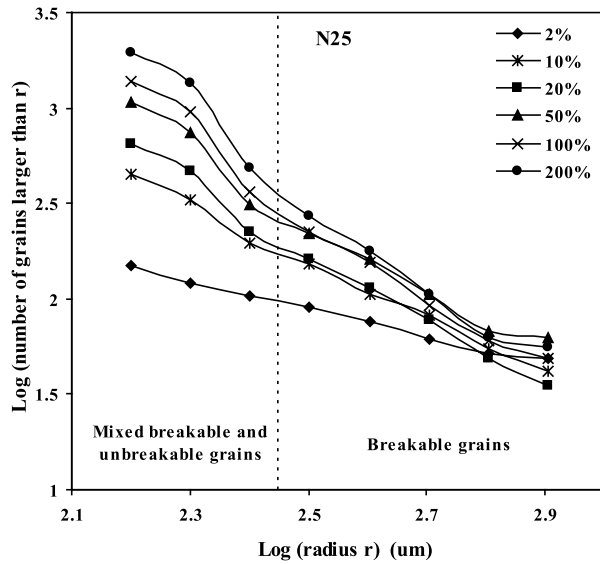


Figure 9. Grain size distribution curves for different shear strains in experiment N25. Breakable grains to the right of dotted line give a relatively unbiased measure of grain size distribution, and D values are estimated from the slopes of these linear portions of the curves. Grain size distributions to the left of dotted line are skewed by the accumulation of unbreakable particles. In this particular example, crushing of gouge grains is a dominant mechanism for grain size reduction, resulting in progressive steepening of PSD curve. At the same time, the total abundance of gouge grains increases, shifting the curve upward.

and finally, to long horizontal linear zones, associated with more localized shear strain (Figures 5d). This correlation suggests that the formation of well-sorted, fine-grained gouge, favored by high σ_n and low σ_{ucs} , facilitates the development of long linear slip zones oriented parallel to, or at low angles to, the fault zone boundaries, i.e., Y shears or low-angle Reidel shears [Scholz, 1990]. In poorly sorted gouges, associated with low σ_n and high σ_{ucs} , slip zones wrap around large grains, probably in less favored orienta-

tions for the simple shear configuration, and thus are short-lived before being replaced by new, more favorably oriented slip zones. Therefore short curved slip zones and distributed deformation are common in less well sorted gouges.

6.2. Gouge Zone Thickness

[35] Several studies have attempted to define the relationships between fault gouge thickness and shear displacement for interpretive purposes in the field [Queener *et al.*, 1965; Scholz, 1987; Power *et al.*, 1988; Scholz, 1990]. Our simulations provide some important tests of such relationships, and demonstrate significant variations with fault rock properties and normal stresses.

[36] The thicknesses of natural and experimental fault gouge zones are primarily a function of the evolutionary wear rates of the fault surfaces. Previous theoretical and experimental studies of gouge zone thickness have demonstrated that the fault wear during continued shearing is characterized by an exponential decay in wear rate during the early stage of sliding, i.e., the “conditioning” stage, and finally, a nearly steady state wear rate later during fault slip [Queener *et al.*, 1965; Scholz, 1987; Power *et al.*, 1988; Scholz, 1990]. Our two stage pattern of wear with increasing shear displacement is consistent with this prediction, i.e., a rapid increase in gouge zone thickness that decays with increasing shear displacement, followed by a more gradual linear increase in the gouge zone thickness (Figure 7). Thus shear displacement is the dominant factor controlling gouge zone thickness. We also found that σ_n and σ_{ucs} can affect this fundamental characteristic of gouge zone growth (Figure 7), e.g., the fast growth stage tends to last longer in the low σ_n and high σ_{ucs} experiments. This is because more strain is accommodated by dilation in the low σ_n and high σ_{ucs} experiments (Figure 3a) (Guo and Morgan, submitted manuscript, 2006), leading to the relatively low wear rates in these experiments.

[37] The high wear rates during the early stages of sliding are thought to be a result of greater roughness of the initial fault surfaces, compared to these later stages of steady state wear [Queener *et al.*, 1965; Scholz, 1990]. This cannot be true for our experiments, however, because the fault surfaces are essentially flat at the onset of our experiments (at least at

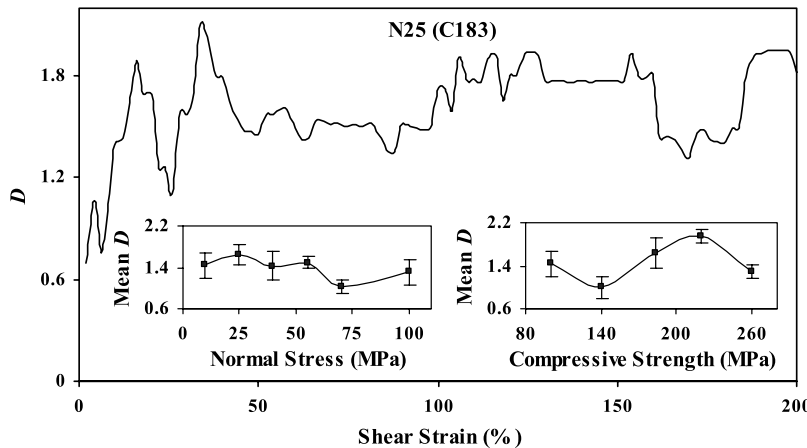


Figure 10. Evolution of fractal dimension D value with shear strain for experiment N25. Insets show variations of mean D value of the slow growth stage with σ_n and σ_{ucs} , respectively. Error bars show the standard deviation. Interpolated lines are fit to data points by eye.

the scale of the largest particles in our simulated fault blocks), whereas they become more irregular and rougher as grains are plucked during sliding (Figures 3a–5a). Instead, the transition in wear rate in our experiments is apparently associated with a transition in shear zone configuration, thickness, and dominant deformation mechanisms. During the early phase of sliding, the fault gouge zone is poorly developed and asperities along the fault surfaces are highly interlocked. This leads to intensive fault block fracture and surface wear (Figure 3). The progressive accumulation of fault gouge gradually changes the dominant deformation mechanisms from wear of the fault surfaces to shearing of the fault gouge, and the fault zone weakens. Eventually, shear strain is accommodated mainly by gouge grain rolling and sliding within a well developed gouge zone, and the irregular fault surfaces are protected from further wear (Figures 5).

[38] Previous studies of the wear process during shear deformation also demonstrated that wear rate is dependent on σ_n and rock bulk strength [Kessler, 1933; Yoshioka, 1986; Scholz, 1987; Wibberley *et al.*, 2000]. Scholz [1987] proposed a theoretical wear model that neglects porosity change within the gouge zone. The model predicts that gouge thickness, T , is linearly proportional to shear displacement, S , and σ_n , and inversely proportional to rock hardness H , i.e.,

$$T = c \sigma_n S / 3H \quad (17)$$

where c is a dimensionless parameter that is expected to be in the range of 0.1–1 for abrasion-dominated wear, and much lower for adhesion-involved wear [Rabinowicz, 1965; Scholz, 1987]. In the direct shear experiments by Yoshioka [1986], the wear rates for sandstone and granite are in rough agreement with the prediction of the model [Scholz, 1987].

[39] The dependence of wear rate on σ_n and σ_{ucs} that we observe, is primarily a function of shear displacement, and appears to be much more complex than that described by Scholz' model. During the fast growth stage, our simulated wear rate tends to increase with increasing σ_n/σ_{ucs} because of increased strain accommodation by dilation (Figure 3a). This observation is qualitatively consistent with Scholz' model that describes a linear dependence of the wear rate on σ_n/σ_{ucs} [Scholz, 1987]. During the slow growth stage, however, the wear rate dependence on σ_n and σ_{ucs} reverses in our simulations. Active deformation mechanisms in our simulated fault gouges suggest that strain is accommodated more efficiently by grain rolling and sliding along long, continuous slip zones within well-sorted, fine-grained gouge in high σ_n and low σ_{ucs} experiments during the slow growth stage (Figures 5c and 5d). Therefore the lower wear rates are achieved in these experiments. Consequently, fault gouge thickness in the low σ_n and/or high σ_{ucs} experiments can exceed those in the high σ_n and/or low σ_{ucs} experiments, if shear displacement is high enough (as shown in Figure 7).

[40] Porosity and dilation may also affect the thickness of our simulated fault gouges. As the gouge porosity under high normal stresses (e.g., about 13% in N100) during the slow growth stage is lower than that of the initial bonded fault block (20%), the reduced thickening rate with increasing σ_n may be partially explained by this compaction. In

real faults, additional gouge consolidation can occur during long periods of stability. This effect is not realized in our simulations. Therefore dilation of our simulated gouge zones may result in greater gouge thickness than in natural faults.

[41] For our results, the dependence of T on σ_n and σ_{ucs} in our experiments can be described by the following best fit equation:

$$\begin{aligned} T &= 1.44(\sigma_n/\sigma_{ucs} + 2.64)S^{0.48} & (S < S^*) \\ T &= 1.44(\sigma_n/\sigma_{ucs} + 2.64)S^{*0.48} \\ &\quad + 0.045(S - S^*)(\sigma_n/\sigma_{ucs})^{-0.42} & (S \geq S^*) \end{aligned} \quad (18)$$

where S is the total shear displacement, and S^* is the critical displacement between the fast growth and slow growth stages, defined as $S^* = 0.032 \sigma_n^{0.25}/\sigma_{ucs}^{-1.25}$. This derived numerical model is conceptually similar to a theoretical wear model suggested by Power *et al.* [1988], in that both models predict a similar evolutionary path of gouge zone thickness, i.e., nonlinear increase followed by a linear, lower rate growth. However, the numerical model presented here more explicitly describes the dependence of gouge zone thickness on σ_n and σ_{ucs} .

[42] For natural faults, the gouge zone thickness to displacement ratios fall between 0.001 and 0.1 [Robertson, 1983]. Equation (18), a best fit to all of the experiments simultaneously, predicts gouge zone thickening rates lie in the range of 0.06 to 0.15 during the slow growth stage (Figure 11), consistent with this observation. However, compared to natural fault zones, the shear displacements in our numerical experiments are relatively short (about 74 mm). Although the thickening rates of our simulated gouge zones are relatively constant during the slow growth stage (Figure 7), further accumulation of fault gouge beyond 200% shear strain (i.e., 74 mm shear displacement) may allow more strain to be accommodated within the gouge zone, thus reducing the fault surface wear rates further. This possibility is supported by the observed exponential decrease in abundances of bond breakage with increasing shear strain in these experiments, which is described in more detail in the companion paper (Guo and Morgan, submitted manuscript, 2006).

6.3. Gouge Grain Size and Size Distribution

[43] The mean gouge grain size in our numerical experiments is primarily controlled by shear displacement, and decreases with increasing shear displacement after reaching a peak value within the first 4% shear strain (i.e., 1.5 mm shear displacement) (Figure 8). This observation is consistent with the results of laboratory experiments, for example, triaxial tests on Sidobre granite that show increasing abundance of smaller grains with increasing shear displacement [Amitrano and Schmittbuhl, 2002]. Our results also show secondary variations in gouge mean grain size with σ_n , and also with σ_{ucs} , i.e., mean gouge grain size tends to decrease with increasing σ_n and with decreasing σ_{ucs} . This is again consistent with lab studies; for example, Wibberley *et al.* [2000] observed that the mean grain size of gouge decreases with increased σ_n in shear box tests on low-porosity sandstone samples. In our numerical experiments, mean gouge grain size depends on the relative activity of two

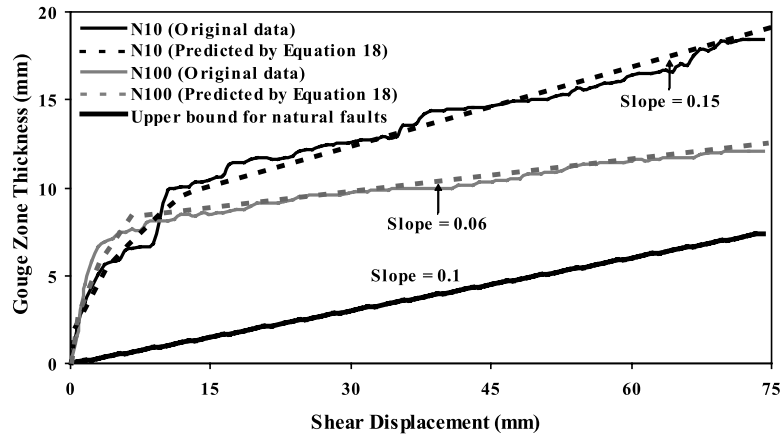


Figure 11. Gouge zone thickness as a function of shear displacement predicted by equation (18). Equation (18) defines the highest and lowest slopes (i.e., ratios of thickness to displacement) during the slow growth stage under the experimental conditions (i.e., normal stress and rock uniaxial compressive strength) for experiments N10 and N100, respectively. The slope predicted by equation (18) is close to the upper bound (i.e., 0.1) observed from natural faults [Robertson, 1983]. The gouge zone thicknesses for experiment N10 and N100 are also plotted as reference for equation (18).

failure mechanisms: fault surface wear and grain comminution (Figures 3b–5b). Initially, high σ_n and low σ_{ucs} facilitate the production of bigger gouge grains by inducing widely spaced and long fractures in the fault blocks with continuing shear displacement, however, high σ_n and low σ_{ucs} also induce substantial grain comminution by crushing (Figures 3a–5a and 3b–5b). In contrast, low σ_n and high σ_{ucs} experiments exhibit less grain plucking, and subsequently low rates of grain comminution. Thus the dependence of mean gouge grain size on σ_n and σ_{ucs} must vary with shear displacement as a result of these variations in wear and comminution rate.

[44] Grain sizes in many natural and artificial fault gouges follow power law grain size distributions, commonly characterized by the fractal dimension D defined in equation (13) [Sammis *et al.*, 1987; Marone and Scholz, 1989; Biegel *et al.*, 1989; Blenkinsop, 1991; An and Sammis, 1994; Storti *et al.*, 2003; Billi *et al.*, 2003; Rawling and Goodwin, 2003; Abe and Mair, 2005]. The grain sizes in our numerical experiments also follow fractal distributions (Figure 9), although the grain size distributions, given in terms of D in two dimensions, vary in step-like fashion with shear displacement, and never evolve to a single steady state value. Primarily, this reflects the unsteady wear of the sliding surfaces, and secondarily the unsteady rate of grain comminution. However, the grain size distribution measured by D also varies with both σ_n and σ_{ucs} because wear and comminution rates are functions of both σ_n and σ_{ucs} .

[45] Our experiments also demonstrate that the spatial and temporal distributions of grain size are not homogeneous in the simulated fault gouge zones (Figures 3b–5b). Large grains tend to be concentrated along the gouge zone boundaries, i.e., the source of new grains, during the slow growth stage. The observed heterogeneity suggests that D values may also vary from the boundary to the gouge zone center in natural fault zones. Similar grain size variations and associated changes in D values have been observed in Death Valley fault rocks and breccia zones [Morgan *et al.*, 1996]. Large particles, defining low D values of ~ 1.7 (two

dimensions), are concentrated in fault damage zones, whereas fine-grained gouge zones, thought to have accommodated intense shear strain [Cowan *et al.*, 2003], yield high D values up to 2.8 in two dimensions. D values measured across fault damage zones, and into the middle of gouge zones in carbonate cataclastic rocks also show similar variations [Storti *et al.*, 2003]. Here, the variability of D value is attributed to a progressive change of the dominant fragmentation mechanism, an increased contribution of surface abrasion, and the variation of particle strength with size and shape, and also increasing shear strain in the center of gouge zone.

6.4. Applicability of the Results

[46] Deformation of our simulated faults under constant normal stresses is similar to aseismic brittle creep in natural fault zones, and may differ from natural seismogenic faults as stress varies during earthquake cycle around these faults. Results presented here were obtained from a range of normal stresses and rock strengths and therefore allow us to infer possible deformation processes of faults experiencing transient stress conditions. Many other deformation conditions, such as slip rate, fault geometry, fault healing, frictional heating, and pore fluid pressure, may also affect fault zone deformation. Their roles have not been explored in this study. Their effects are expected to be studied in our ongoing and future DEM simulations.

7. Conclusions

[47] DEM simulations of the growth of fault gouge zones demonstrate that gouge zone evolution involves two distinct stages, i.e., fast growth and slow growth, associated with transitions in the dominant deformation mechanisms and in shear zone configuration. During the first stage, the gouge zones are poorly developed, and deformation is characterized by the development of tensile fractures parallel or subparallel to σ_1 in the fault blocks. Fracture of the wall rock is the dominant deformation structure, and is more

significant in high σ_n and low σ_{ucs} experiments. Shear displacement is mainly accommodated by wear of the fault zone. With increasing gouge zone thickness, grain sliding and rotation are enhanced while fracturing is reduced. The beginning of the second evolutionary stage is marked by the significant reduction in wear rate and the formation of a well-developed gouge zone at about 20% shear strain (i.e., 7.4 mm shear displacement). Deformation during this later stage is characterized by the development of transient slip zones within the fault gouge. Shear strain is mainly accommodated by shearing within the gouge through grain sliding, rolling, and crushing. Gouge grain sorting affects the types and geometries of the shear structures that develop. The formation of well-sorted, fine-grained gouge favors the development of long linear horizontal and subhorizontal slip zones.

[48] The rate of gouge zone thickening in our numerical experiments decreases exponentially during the fast growth stage and becomes approximately constant during the slow growth stage. The transition indicates that the gouge zone reaches a critical thickness that allows strain to be accommodated more efficiently within gouge. The dependence of the gouge zone thickness on σ_n and σ_{ucs} varies with shear displacement. During the fast growth stage, the rate of gouge zone thickening increases with increasing σ_n and decreasing σ_{ucs} . This is because more strain is accommodated by dilation in low σ_n and high σ_{ucs} experiments instead of surface wear. The dependency reverses during the slow growth stage. This is because more strain is accommodated by grain rolling and sliding along well-developed slip zones within well-sorted, fine-grained gouge in high σ_n and low σ_{ucs} experiments. The entire wear process can be described by a wear model (i.e., equation (18)) that predicts thicker fault gouge in high σ_{ucs} shear zones deformed under low σ_n if shear displacements are high enough.

[49] Mean gouge grain size in our numerical experiments is primarily dependent on shear strain, and decreases exponentially with increasing shear displacement after reaching a peak value within the first 4% shear strain (i.e., 1.5 mm shear displacement). Mean grain size also shows a secondary dependence on σ_n and σ_{ucs} and tends to decrease with increasing σ_n and decreasing σ_{ucs} . Grains in our simulated fault gouges obey a fractal size distribution. The 2-D D values fall into a wide range from 0.6 to 2.4, and vary unsystematically with shear displacement, σ_n , and σ_{ucs} . Our results demonstrate that surface wear preferentially generates large grains along the gouge zone boundaries, causing fluctuations in grain size distribution during a simulation. The properties (i.e., abundance and size) of the wear products are strongly dependent on shear displacement, σ_n , and σ_{ucs} . Therefore wear, together with grain comminution, plays an important role in producing the characteristics of the grain size distribution observed in our numerical experiments.

[50] **Acknowledgments.** We thank David Sparks and Stephen Cox for their thoughtful comments on the manuscript. This work was funded by National Science Foundation grant EAR-0337757 and the Southern California Research Center. SCEC is funded by NSF Cooperative Agreement EAR-0106924 and USGS Cooperative Agreement 02HQAG0008. This is SCEC contribution 1117. Guo was also partially supported by a Shell Graduate Fellowship. Computing facilities were made available through the Rice Center for Computational Geophysics.

References

- Abe, S., and K. Mair (2005), Grain fracture in 3D numerical simulations of granular shear, *Geophys. Res. Lett.*, **32**, L05305, doi:10.1029/2004GL02123.
- Amitrano, D., and J. Schmittbuhl (2002), Fracture roughness and gouge distribution of a granite shear band, *J. Geophys. Res.*, **107**(B12), 2375, doi:10.1029/2002JB001761.
- An, L., and C. G. Sammis (1994), Particle size distribution of cataclastic fault materials from southern California: A 3-D study, *Pure Appl. Geophys.*, **143**, 203–227.
- Anderson, J. L., R. H. Osborne, and D. F. Palmer (1980), Petrogenesis of cataclastic rock within the San Andreas fault zone of southern California, *Tectonophysics*, **67**, 221–229.
- Anderson, J. L., R. H. Osborne, and D. F. Palmer (1983), Cataclastic rock of the San Gabriel fault—An expression of deformation at deeper crustal levels in the San Andreas fault zone, *Tectonophysics*, **98**, 209–251.
- Anthony, J. L., and C. Marone (2005), Influence of particle characteristics on granular friction, *J. Geophys. Res.*, **110**, B08409, doi:10.1029/2004JB003399.
- Attewell, P. B., and I. W. Farmer (1976), *Principles of Engineering Geology*, Chapman and Hall, London.
- Beeler, N. M., T. E. Tullis, and J. D. Weeks (1996), Frictional behavior of large displacement experimental faults, *J. Geophys. Res.*, **101**, 8697–8715.
- Biegel, R. L., C. S. Sammis, and J. H. Dieterich (1989), The frictional properties of a simulated gouge having a fractal particle distribution, *J. Struct. Geol.*, **11**, 827–846.
- Billi, A., F. Salvini, and F. Storti (2003), The damage zone-fault core transition in carbonate rocks: Implications for fault growth, structure and permeability, *J. Struct. Geol.*, **25**, 1779–1794.
- Blenkinsop, T. G. (1991), Cataclasis and processes of particle size reduction, *Pure Appl. Geophys.*, **136**, 59–86.
- Byerlee, J., and R. Summers (1976), A note on the effect of fault gouge thickness on fault stability, *Int. J. Rock Mech. Min. Sci. Geomech. Abstr.*, **13**, 35–36.
- Byerlee, J., V. Mjachkin, R. Summers, and O. Voevoda (1978), Structures developed in fault gouge during stable sliding and stick-slip, *Tectonophysics*, **44**, 161–171.
- Chester, F. M., and J. M. Logan (1987), Composite planar fabric of fault gouge from the Punchbowl Fault, California, *J. Struct. Geol.*, **9**, 621–634.
- Cowan, D. S., T. T. Cladouhos, and J. K. Morgan (2003), Structural geology and kinematic history of rocks formed along low-angle normal faults, Death Valley, California, *Geol. Soc. Am. Bull.*, **115**, 1230–1248.
- Cundall, P. A., and O. D. L. Strack (1979), A discrete numerical model for granular assemblies, *Geotechnique*, **29**, 47–65.
- Dieterich, J. H. (1981), Constitutive properties of faults with simulated gouge, in *Mechanical Behavior of Crustal Rocks*, *Geophys. Monogr. Ser.*, vol. 24, edited by N. L. Carter, M. Friedman, J. M. Logan, and D. W. Stearns, pp. 103–120, AGU, Washington, D. C.
- Engelder, J. T. (1974), Cataclasis and the generation of fault gouge, *Geol. Soc. Am. Bull.*, **85**, 1515–1522.
- Engelder, J. T., J. M. Logan, and J. Handin (1975), The sliding characteristics of sandstone on quartz fault-gouge, *Pure Appl. Geophys.*, **113**, 69–86.
- Gu, Y., and T. F. Wong (1994), Development of shear localization in simulated quartz gouge: Effects of cumulative slip and gouge particle size, *Pure Appl. Geophys.*, **143**, 387–423.
- Guo, Y., and J. K. Morgan (2004), Influence of normal stress and grain shape on granular friction: Results of discrete element simulations, *J. Geophys. Res.*, **109**, B12305, doi:10.1029/2004JB003044.
- Guo, Y., and J. K. Morgan (2006), The frictional and micromechanical effects of grain comminution in fault gouge from distinct element simulations, *J. Geophys. Res.*, **111**, B12406, doi:10.1029/2005JB004049.
- Heermance, R., Z. K. Shipton, and J. P. Evans (2003), Fault structure control on fault slip and ground motion during the 1999 rupture of the Chelungpu fault, Taiwan, *Bull. Seismol. Soc. Am.*, **93**, 1034–1050.
- Johnson, K. L. (1985), *Contact Mechanics*, Cambridge Univ. Press, Cambridge, U. K.
- Kessler, D. W. (1933), Wear resistance of natural stone flooring, *U.S. Bur. Stand. Res. Pap.*, **RP612**, 635–648.
- Knipe, R. J., and S. H. White (1979), Deformation in low grade shear zones in the Old Red Sandstone, SW Wales, *J. Struct. Geol.*, **1**, 53–66.
- Lin, A. (2001), S-C fabric developed in cataclastic rocks from Nojima fault zone, Japan and their implications for tectonic history, *J. Struct. Geol.*, **23**, 1167–1178.
- Logan, J. M., M. Friedman, N. Higgs, C. Dengo, and T. Shimamoto (1979), Experimental studies of simulated gouge and their application to studies of natural fault zones, *Proceedings of Conference VIII—Analysis of Actual*

- Fault Zones in Bedrock*, U.S. Geol. Surv. Open File Rep., 79–1239, 305–343.
- Logan, J. M., C. A. Dengo, N. G. Higgs, and Z. Z. Wang (1992), Fabrics of experimental fault zones: Their development and relationship to mechanical behavior, in *Fault Mechanics and Transport Properties in Rocks*, edited by B. Evans and T. F. Wong, pp. 33–67, Academic, New York.
- Mair, K., K. M. Frye, and C. Marone (2002), Influence of grain characteristics on the friction of granular shear zones, *J. Geophys. Res.*, 107(B10), 2219, doi:10.1029/2001JB000516.
- Marone, C., and C. H. Scholz (1989), Particle-size distribution and microstructures within simulated fault gouge, *J. Struct. Geol.*, 11, 799–814.
- Marone, C., C. B. Raleigh, and C. H. Scholz (1990), Frictional behavior and constitutive modeling of simulated fault gouge, *J. Geophys. Res.*, 95, 7007–7025.
- Mindlin, R. D., and H. Deresiewicz (1953), Elastic spheres in contact under varying oblique forces, *Trans. ASME J. Appl. Mech.*, 20, 327–344.
- Monzawa, N., and K. Otsuki (2003), Commminution and fluidization of granular fault materials; implications for fault slip behavior, *Tectonophysics*, 367, 127–143.
- Mora, P., and D. Place (1998), Numerical simulation of earthquake faults with gouge: Toward a comprehensive explanation for the heat flow paradox, *J. Geophys. Res.*, 103, 21,067–21,089.
- Mora, P., and D. Place (1999), The weakness of earthquake faults, *Geophys. Res. Lett.*, 26, 123–126.
- Morgan, J. K. (1999), Numerical simulations of granular shear zones using the distinct element method, 2: Effects of particle size distribution and interparticle friction on mechanical behavior, *J. Geophys. Res.*, 104, 2721–2732.
- Morgan, J. K., and M. S. Boettcher (1999), Numerical simulations of granular shear zones using the distinct element method: 1. Shear zone kinematics and the micromechanics of localization, *J. Geophys. Res.*, 104, 2703–2719.
- Morgan, J. K., T. T. Cladouhos, K. M. Scharer, D. S. Cowan, and P. Vrolijk (1996), Fractal particle size distributions in Death Valley fault zones: Controls on mechanics and kinematics of fault rocks, *Eos Trans. AGU*, 77, 717.
- Morrow, C. A., and J. D. Byerlee (1989), Experimental studies of compaction and dilatancy during frictional sliding on faults containing gouge, *J. Struct. Geol.*, 11, 815–825.
- Morrow, C., B. Radney, and J. Byerlee (1992), Frictional strength and the effective pressure law of montmorillonite and illite clays, in *Fault Mechanics and Transport Properties of Rocks: A Festschrift in Honor of W. F. Brace*, edited by B. Evans and T. F. Wong, pp. 69–88, Academic, San Diego, Calif.
- Power, W. L., T. E. Tullis, and J. D. Weeks (1988), Roughness and wear during brittle faulting, *J. Geophys. Res.*, 93, 15,268–15,278.
- Queener, C. A., T. C. Smith, and W. L. Mitchell (1965), Transient wear of machine parts, *Wear*, 8, 391–400.
- Rabinowicz, E. (1965), *Friction and Wear of Materials*, John Wiley, New York.
- Rawling, G. C., and L. B. Goodwin (2003), Cataclasis and particulate flow in faulted, poorly lithified sediments, *J. Struct. Geol.*, 25, 317–331.
- Robertson, E. G. (1983), Relationship of fault displacement to gouge and breccia thickness, *Mineral. Eng.*, 35, 1426–1432.
- Rutter, E. H., R. H. Maddock, S. H. Hall, and S. H. White (1986), Comparative microstructures of natural and experimentally produced clay-bearing fault gouges, *Pure Appl. Geophys.*, 124, 3–30.
- Saffer, D. M., and C. Marone (2003), Comparison of smectite- and illite-rich gouge frictional properties: Application to the updip limit of the seismogenic zone along subduction megathrusts, *Earth Planet. Sci. Lett.*, 215, 219–235.
- Saffer, D. M., K. M. Frye, C. Marone, and K. Mair (2001), Laboratory results indicating complex and potentially unstable frictional behavior of smectite clay, *Geophys. Res. Lett.*, 28, 2297–2300.
- Sammis, C. G., and R. H. Osborne (1982), Textural and petrographic modal analysis of gouge from a depth of 165 m in the San Andreas fault zone, *Eos Trans. AGU*, 68, 1109.
- Sammis, C. G., R. H. Osborne, J. L. Anderson, M. Banerdt, and P. White (1986), Self-similar cataclasis in the formation of fault gouge, *Pure Appl. Geophys.*, 124, 53–78.
- Sammis, C. G., G. King, and R. Biegel (1987), The kinematics of gouge deformation, *Pure Appl. Geophys.*, 125, 777–812.
- Scholz, C. H. (1987), Wear and gouge formation in brittle faulting, *Geology*, 15, 493–495.
- Scholz, C. H. (1990), *The Mechanics of Earthquakes and Faulting*, Cambridge Univ. Press, New York.
- Scholz, C. H., P. Molnar, and T. Johnson (1972), Detailed studies of frictional sliding of granite and implications for the earthquake mechanism, *J. Geophys. Res.*, 77, 6392–6406.
- Storti, F., A. Billi, and F. Salvini (2003), Particle size distributions in natural carbonate fault rocks; insights for non-self-similar cataclasis, *Earth Planet. Sci. Lett.*, 206, 173–186.
- Tullis, T. E., M. L. Blanpied, and J. D. Weeks (1989), The velocity dependence of granite friction with and without simulated gouge, *Eos Trans. AGU*, 70, 1302.
- Turcotte, D. L. (1986), Fractals and fragmentation, *J. Geophys. Res.*, 91, 1921–1926.
- Wibberley, C. A. J., J. P. Petit, and T. Rives (2000), Micromechanics of shear rupture and the control of normal stress, *J. Struct. Geol.*, 22, 411–427.
- Wilson, B., T. Dewers, Z. Reches, and J. N. Brune (2005), Particle size and energetics of gouge from earthquake rupture zones, *Nature*, 434, 749–752.
- Yoshioka, N. (1986), Fracture energy and the variation of gouge and surface roughness during frictional sliding of rock, *J. Phys. Earth*, 34, 335–355.

Y. Guo and J. K. Morgan, Department of Earth Science, Rice University, 6100 Main Street, Houston, TX 77005, USA. (yonggui@rice.edu)